Evaluation of global NWP data on Convection Environment over the Data-Sparse Northern South China Sea by Long-Term Observations

Ling Huang*[1], Zhiyong Meng[2], Murong Zhang[3]

[1]*Institute of Tropical and Marine Meteorology, CMA, Guangzhou, China*

[2]*Department of Atmospheric and Oceanic Sciences, School of Physics, and China Meteorological Administration Tornado Key Laboratory, Peking University, Beijing, China*

[3] *State Key Laboratory of Marine Environmental Science, Center for Marine Meteorology and Climate Change, College of Ocean and Earth Sciences, Xiamen University, Fujian, China*

ABSTRACT

The coastal regions of southern China experience the country's most frequent convective weather. Accurately representing the low-level upstream atmospheric state over the data-sparse South China Sea (SCS) is crucial for reliable convection predictions in numerical models. Utilizing ten years of radiosonde observations launched over the SCS, this study presents the upstream offshore convective environments and evaluates the global model data performance including NCEP FNL, ERA5, CRA-40, JRA-3Q, and MERRA-2. Results show that thermodynamic state variables such as temperature and humidity exhibit greater biases than kinetic variables, particularly at low levels. Deeper-layer parameters exhibit smaller uncertainties, especially wind-related variables, while moisture-related parameters have the largest uncertainties, compared to shallower-layer parameters. All model data tend to underestimate the conditional instability and equilibrium level, while overestimating the condensation level, storm relative helicity (SRH), with minimal bias in lapse rate, convective

*Corresponding author: Ling HUANG (huangl_atmos@foxmail.com)

inhibition, vertical wind shear (VWS) and mean winds. These biases primarily arise from the model data's underestimation of temperature and moisture below 700 hPa and lower wind speeds below 950 hPa. Among the global models, CRA-40 performs best in dynamic parameters, with highest correlation and lowest mean absolute error in low-level winds, SRH, VWS, and mean winds. ERA5 excels in thermodynamic parameters. Additional convective-permitting numerical experiments indicate that minor initial condition errors over the upstream ocean significantly affect coastal rainfall production. The rainfall production on windward coasts is most sensitive to the low-level air temperature errors during nocturnal hours, while the rainfall over the PRD is most sensitive to the low-level wind errors.

Key words: Radiosonde, convective environments, rainfall, Northern South China Sea

https://doi.org/10.1007/s00376-025-5287-7

Article Highlights:

- NWP data exhibit systematic bias under 950 hPa, with positive biases in V and negative biases in U, Q, and T.
- NWP data are least reliable for moisture-related parameters, followed by temperature-related parameter, and most reliable for wind-related parameters.
- CRA-40 performs best for wind-related parameters, while ERA5 excels in moisture- and temperature-related parameters.
- The rainfall production on windward coasts is most sensitive to the low-level air temperature errors during nocturnal hours.

1. Introduction

Located to the north of the South China Sea, the southern China coasts are densely populated and economically vital, making them highly vulnerable to extreme weather events like heavy rainfall (Fig. 1a), typhoons, and storm surges, particularly from April to September (Sun et al. 2019; Fu et al. 2022). Accurate forecasts are crucial for safeguarding lives, and reducing economic losses. Previous studies have demonstrated that upstream environment over Northern South China Sea (NSCS) significantly influence downstream coastal weather, especially under monsoonal flow conducive to severe convection (Du et al. 2019). Understanding the low-level upstream atmospheric state over the data-sparse NSCS is critical for unrevealing mechanisms behind severe weather formation and development. An accurate representation of this state in numerical models is vital for enhancing the reliability of convection forecasts in downstream coastal regions.

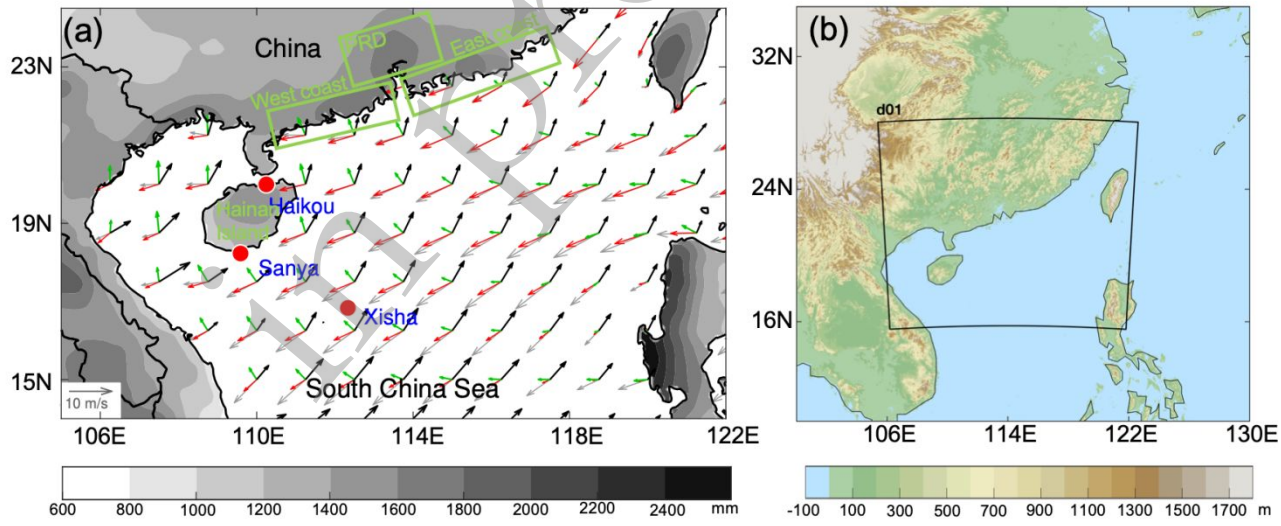

Fig. 1. (a) Distribution of seasonal wind vectors at 925 hPa of March to May (green vectors), June to August (black vectors), September to November (red vectors) and December to February (grey vectors) from 2014 to 2023. The color shadings indicate the annual rainfall averaged from 2014 to 2023, obtained from IMERG. The red dots indicate the location of soundings. The green rectangles indicate the hot spot of precipitation over the south coast China: the west coast, the east coast, and the pearl river delta region (PRD). (b) Domain and Topography of the simulations.

Radiosonde observations have been widely used to study regional convective climatology, but

61 they are spatially and temporally limited (Bao et al. 2013; Allen and Tippett 2015; Tippett et al. 2016;
62 Taszarek et al. 2017, 2018; Virman et al. 2021). Numerical weather prediction (NWP) models provide
63 a more comprehensive, high-resolution four-dimensional view of the atmosphere and are particularly
64 beneficial for analyzing sensitive parameters like storm-relative helicity (SRH) or CAPE (Markowski
65 et al. 1998). Spatiotemporal climatology of severe convective environments based on NWP data have
66 been investigated globally (e.g., Chen et al. 2020; Taszarek et al. 2018, 2020, 2021; Rädler et al.
67 2018; Varga et al. 2022), which revealed regional dependent features across continentals. For instance,
68 Taszarek et al. (2018) noted CAPE underestimation in eastern Europe and overestimation in
69 Mediterranean. Over mainland China, Wu et al. (2024) observed CAPE overestimation 2 h before the
70 rainfall onset. These findings underscore the need to assess NWP data quality for specific regions
71 before applying them to research or forecasting.

72 While satellite data have enhanced upper and mid-tropospheric analysis, their reliability in
73 resolving low-level thermodynamic and dynamic profiles—critical for understanding local
74 convective environments—remains uncertain due to sparse observational constraints (e.g., Davis et
75 al. 2017; Manney et al. 2017). For thermodynamic parameters, large errors in low-level temperature
76 and moisture fields are noticed in NWP datasets, such as the ERA-interim (Allen and Karoly 2014),
77 NCEP/NCAR reanalysis data (Lee 2002), and RUC-2 data (Thompson et al. 2003). For dynamics,
78 Taszarek et al. (2018) found underestimation of low-level vertical wind shear in ERA-Interim
79 compared to sounding. Similarly, WRF simulations show biases in low-level jet (LLJ) placement and
80 wind speed over SCS and inland regions (Zhang and Meng 2019). Yin et al. (2023) reported larger
81 RMSEs in ERA-Interim U and V at low levels over East Asia. Uncertainty persists regarding the

quantitative impact of low-level environmental errors on the convective environment.

Over the past two decades, the convective environments (Allen and Karoly 2014; King and Kennedy 2019; Li et al. 2020; Taszarek et al. 2021; Varga et al. 2022; Pilguj et al. 2022) in global NWP datasets and comparisons among various NWP datasets (Taszarek et al. 2021; Varga and Breuer 2022) have been assessed across regions. Varga and Breuer (2022) found that while WRF captures the seasonal cycle of thunderstorm predictors over Central Europe, its errors are higher than ERA5. Taszerk et al. (2021) analyzed millions of rawinsonde profiles against ERA5 and MERRA-2, finding ERA5 is generally more accurate. The ERA5 data are demonstrated to have higher correlations and lower mean absolute errors than MERRA-2 in turns of convective parameters and their trends (Pilguj et al. 2022). Each of the evaluated NWP data showed strengths and weaknesses, but broadly, they were found to adequately replicate the background convective environments.

Recently released reanalyses—JRA-3Q (Kosaka et al. 2024) and CRA-40 (Liu et al. 2023)—show promising improvements but have not yet been comprehensively assessed for convective environments. Harada et al. (2021) presents early results of evaluation of JRA-3Q, showing its enhanced precipitation representation, reduced tropical dry biases, and improved diabatic heating, compared to its previous version (JRA-55), likely due to better physical parameterizations (Kosaka et al. 2024). CRA-40, developed by the China Meteorological Administration, shows some advantages over China in terms of precipitation (Zhou et al. 2023), surface air temperature (Yang et al. 2021), humidity (Zhang et al. 2021), wind speed (Shen et al. 2022), tropic divergent kinetic energy (Li et al. 2023), and Asian subtropical westerly jet stream (Yu et al. 2021). These results suggest that the improvement of CAR-40 and JRA-3Q allows for an excellent representation of weather system;

however, these have not yet to be explored for convective environments.

While global NWP datasets can replicate temperature, specific humidity, and wind profiles, biases remain nontrivial and may exceed regional climate signal magnitudes (e.g., Bao et al. 2013; Pilguj et al. 2022). The effects of these initial and boundary condition errors on high-impact weather events like heavy rainfall have been explored in case studies using data assimilation and ensemble forecasts (e.g., Toptill and Kirshbaum 2022), including the torrential rainfall over the South China (e.g., Gao et al. 2022; Bao et al. 2023). However, the climatological impact of such errors on convection remains poorly understood.

Convective predictability over southern China coasts remains relatively low (e.g., Huang and Luo 2017). Given the NSCS's importance to coastal convection (e.g., Ding and Chan 2005), this study aims to 1) investigate the climatology of convective parameters over the NSCS using 10 years of high-quality sounding data, 2) evaluate convective parameters from five widely used NWP datasets, and 3) investigate how initial and boundary condition errors in these datasets influence convection prediction from a climatological perspective. Section 2 introduces the datasets. Section 3 presents the evaluation through basic state quantities, thermodynamic parameters, and dynamic parameters. Section 4 explores the impact of initial and boundary condition errors on coastal convections. The summary and discussion are presented in section 5.

2. Data and Methods

2.1 Radiosonde observations

The vertical atmospheric profiles were derived from three sounding over the northern South China Sea (Fig. 1a). For year 2014−2023 all available measurements accounts for 20793 soundings.

However, to ensure the quality of the sounding data, strict quality-control procedures, including consistency check, discrete value check, monotonicity check, stagnation value check, and limit value check, were performed. Specifically, the limit values for pressure, temperature, and wind speed are 0.1~1050 hPa, -100~60 ^{o}C, and 0~180 m s^{-1}. Given the inconsistency between the sounding and NWP data profile levels, the coarser soundings profiles are interpolated into the denser levels[1] through spline interpolation. Of noted is that the data under 925 hPa is missing for Sanya station since its balloon drop point started from 419.4 m above sea level. Thus, the data at 1000, 975, and 950 hPa are set to missing value for Sanya profiles.

Of noted is that two of them (Haikou and Xisha stations) have been incorporated into the reanalysis processes through the Global Telecommunication System program. Even though NWP reanalysis combines observations and numerical models to produce the best estimate of the atmospheric state, simulated biases inevitably persist due to the constraints of physical balance during the data assimilation process (Taszarek et al. 2021). A possible reason is that the soundings are launched over land in a small island, whereas the NWP data may represent the corresponding grid point as more oceanic (Virman et al. 2021).

2.2 NWP datasets

Five modern global NWP datasets, include CRA-40 from Chinese Meteorological Administration (Liu et al. 2023), JRA-3Q from Japanese Meteorological Administration (Kosaka et al. 2024), FNL from the NCEP Global Forecast System (GFS; NCEP 2000), MERRA-2 from NASA's Global Modeling and Assimilation Office (GMAO; Gelaro et al. 2017), and ERA-5 from ECMWF (Hersbach et al. 2020). CRA-40, China's first-generation reanalysis, offers 6-hourly data at 34 km

resolution with 64 vertical levels, including 8 below 2 km. JRA-3Q provides 40 km resolution and 100 vertical layers, with 23 below 2 km. FNL offers 1°×1° data every 6 hours with 26 vertical levels, 6 of which are below 2 km. MERRA-2 has 0.5°×0.625° resolution, 3-hour intervals, and 72 levels (14 below 2 km). ERA5 features 0.25° resolution, and 137 vertical levels, including 28 in the lowest 2 km. To enable comparison, a set of standard pressure levels[1], with a focus on low-level layers, is used across all datasets. Coarser data, such as FNL, are interpolated into these standard levels using spline interpolation. The soundings of the NWP are derived from the grid points nearest to the station, which show resemble profiles to the nearby environment (not showed).

2.3 Convective parameters

The parameters evaluated were selected based on commonly used indices in severe thunderstorm environments (e.g., Taszarek et al. 2021). These include thermodynamic parameters like surface-based (SB) parcel parameters (SBCAPE, SBCIN, and LCL) and lapse rates (LR) between different bulk layers ($LR_{0\text{-}1km}$, $LR_{0\text{-}3km}$, and $LR_{500\text{-}700hPa}$), as well as dynamic parameters such as vertical wind shear ($VWS_{0\text{-}1km}$, $VWS_{0\text{-}3km}$, $VWS_{0\text{-}6km}$), storm relative helicity ($SRH_{0\text{-}1km}$, $SRH_{0\text{-}3km}$), and mean wind ($MW_{0\text{-}1km}$, $MW_{0\text{-}3km}$, and $MW_{0\text{-}6km}$; Table 1). VWS and MW were calculated using wind differences or averages between 10 m and the heights of 1, 3, and 6 km AGL. All the parameters are computed using the same script across the datasets (sounding, ERA5, CRA-40, MERRA-2, JRA-3Q, and FNL) to ensure consistency. Due to limited data is below 925 hPa at the Sanya station, its surface-based parameters were excluded.

Table 1. List of some common abbreviation and acronyms.

[1] The pressure levels used in the current study are 1000, 975, 950, 925, 900, 875, 850, 825, 800, 775, 750, 700, 650, 600, 500, 400, 300, 200, 100 hPa.

Abbreviation	Stands for	units
AGL	Above ground level	m
SBCAPE	surface-based convective available potential energy	J kg^{-1}
SBCIN	surface-based convective Inhibition	J kg^{-1}
LCL	level of free convection	m
$LR_{0\text{-}1km}$	lapse rate from 0 to 1 km	K m^{-1}
$LR_{0\text{-}3km}$	lapse rate from 0 to 3 km	K m^{-1}
$LR_{700\text{-}500hPa}$	lapse rate from 700 to 500 hPa	K hPa^{-1}
$VWS_{0\text{-}1km}$	vertical wind shear between 0 and 1 km AGL	m s^{-1}
$VWS_{0\text{-}3km}$	vertical wind shear between 0 and 3 km AGL	m s^{-1}
$VWS_{0\text{-}6km}$	vertical wind shear between 0 and 6 km AGL	m s^{-1}
$SRH_{0\text{-}1km}$	storm relative helicity between 0 and 1 km	m^2 s^{-2}
$SRH_{0\text{-}3km}$	storm relative helicity between 0 and 3 km	m^2 s^{-2}
$MW_{0\text{-}1km}$	mean wind speed between 0 and 1 km	m s^{-1}
$MW_{0\text{-}3km}$	mean wind speed between 0 and 3 km	m s^{-1}
$MW_{0\text{-}6km}$	mean wind speed between 0 and 6 km	m s^{-1}

2.4 Design of semi-idealized numerical experiments

Various NWP models are expected to introduce varying degrees of bias. To assess how these biases, affect coastal convection and its associated rainfall in downstream regions, periodic convection-permitting simulations were conducted. These simulations aim not to replicate specific events but to assess how background state errors influence general rainfall pattern during the rainy season. Periodic simulations use averaged initial and boundary conditions to isolate the impact of these errors while preserving daily diurnal cycles, such as land-sea breezes. The control experiment (CTL) uses a 10-day simulation with the 549-day-averaged FNL data (from April 1st to September 30th, 2020-2023) as initialization at 0000 UTC and repeated boundary conditions at 0000, 0600, 1200, and 1800 UTC. This setup removes temporal variability while retaining daily diurnal features, enabling simulation of typical diurnal driven precipitation, as used in previous studies (e.g., Sun and Zhang 2012; Chen et al. 2016). It should be noted that the purpose of these simulations is to

177 investigate how different error types affect convection and associated precipitation. The FNL has
178 known typical errors, especially for low-level dynamic parameters (section 3.2.1), making it a suitable
179 choice for the initial and boundary conditions in our periodic simulation.

180 Simulations use the WRF-ARW model (V4.5; Skamarock et al. 2008) over a single domain
181 covering South China and the NSCS, with 400 × 330 horizontal grid points at 4-km grid spacing
182 (Figure 1b) and 51 vertical layers up to 50 hPa. Key physics schemes include YSU (Hong et al. 2006),
183 Noah-MP (Niu et al., 2011), 5-layer thermal diffusion (Chen and Dudhia, 2003), WDM6 (Hong et
184 al., 2004), Grell-Devenyi ensemble (Grell and Devenyi, 2002), and RRTMG (Mlawer et al., 1997)
185 for both longwave and shortwave radiations.

186 Sensitivity experiments of the semi-idealized periodic simulations were designed by subtracting
187 vertical biases in U, V, T, and RH, either individually or combined, over the NSCS. These errors,
188 based on April-September 2020-2023 station-mean profiles (similar to April-September 2014-2023),
189 were further incorporated into the oceanic region. Subtracting these climatological errors helps align
190 model input with observation. Five sensitivity experiments were conducted (Table 2), including the
191 "add_T_RH_U_V" experiment to test the combined effects and "add_T" to isolate temperature
192 influence.

193 **Table 2.** Design of the sensitivity experiments

EXP	Experiment design
CTL	Simulation using periodic initial and boundary conditions averaged from April to September in 2020-2023
add_T_RH_U_V	Similar to CTL, but the initial and boundary conditions over the ocean are introduced errors of T, RH, U, V from 1000-700 hPa
add_T	Similar to add_T_RH_U_V, but only the temperature errors are introduced
add_RH	Similar to add_T_RH_U_V, but only the humidity errors are introduced
add_T_RH	Similar to add_T_RH_U_V, but only the humidity and temperature errors are

	introduced
add_U_V	Similar to add_T_RH_U_V, but only the wind errors are introduced

3. Results

3.1 General characteristics of atmospheric states calculated using Radiosondes

3.1.1. Basic states

Figure 2 presents the vertical profiles and seasonal variations of radiosonde-derived meteorological variables. From April to September, low-level winds are characterized by southerly components, which strengthen in April, peak in June with the South China Sea monsoon outbreaks (Li et al. 1996), and weaken by July (Fig. 2a). Temperature and humidity also vary monthly, with cooler, drier condition before monsoon and warming/humidifying as it progresses (Figs. 2e-2f). Zonal wind shifts from easterly (April-May) to westerly (June-August), then back to easterly in September (Fig. 2b), causing a total wind direction transitions from southeasterly to southwesterly (Fig. 2c). A strong low-level jet appears near 950 hPa from April to August (Fig. 2d), linked to intensified the southerlies (Fig. 2a). This pattern suggests low-level air affecting coastal South China originates mainly from the NSCS (Fig. 1a).

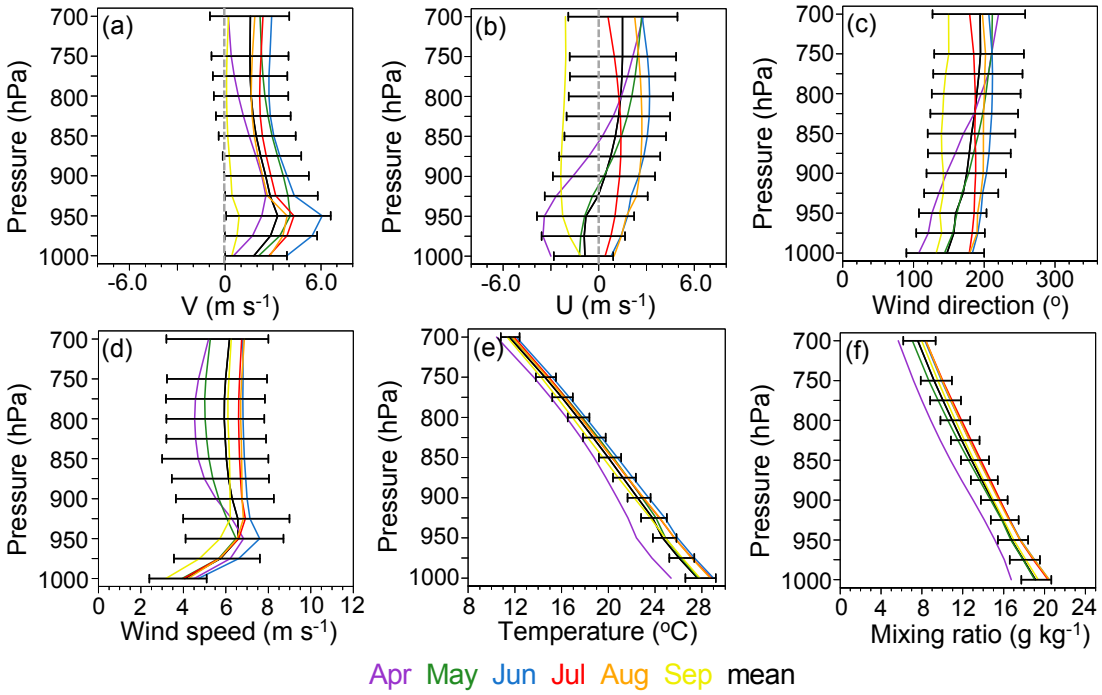

Fig. 2. Vertical profiles of average (a) meridional wind (m s^{-1}), (b) zonal wind (m s^{-1}), (c) wind direction (°), (d) total wind speed (m s^{-1}), (e) temperature (°C), (f) water vapor mixing ratio (g kg^{-1}) obtained from the radiosonde observations. The error bars show the outliers (i.e., 10th and 90th percentiles are whiskers).

3.1.2. Convective environments

Situated in the tropical ocean, the NSCS has high conditional instability, with a mean SBCAPE reaching 1500 J kg^{-1}, much higher than Europe and North America (250 J kg^{-1}; Taszarek et al. 2021). The SBCAPE rise with the onset of monsoonal flow in late May, peaks during the outbreaks of monsoonal flow in June, and remains high in July and August (Fig. 3a). As monsoonal flow strengthen, SBCIN drops below 50 J kg^{-1} (Fig. 3b), and $LR_{0\text{-}3km}$ rise to ~5.5 °C km^{-1} from June onward (Fig. 3c). LCL values, though lower than Europe and North American (Taszarek et al. 2021), show little monthly change (Fig. 3d). This combination of high SBCAPE, moderate SBCIN, low LCL and steep LR create favorable conditions for convection with lower cloud base.

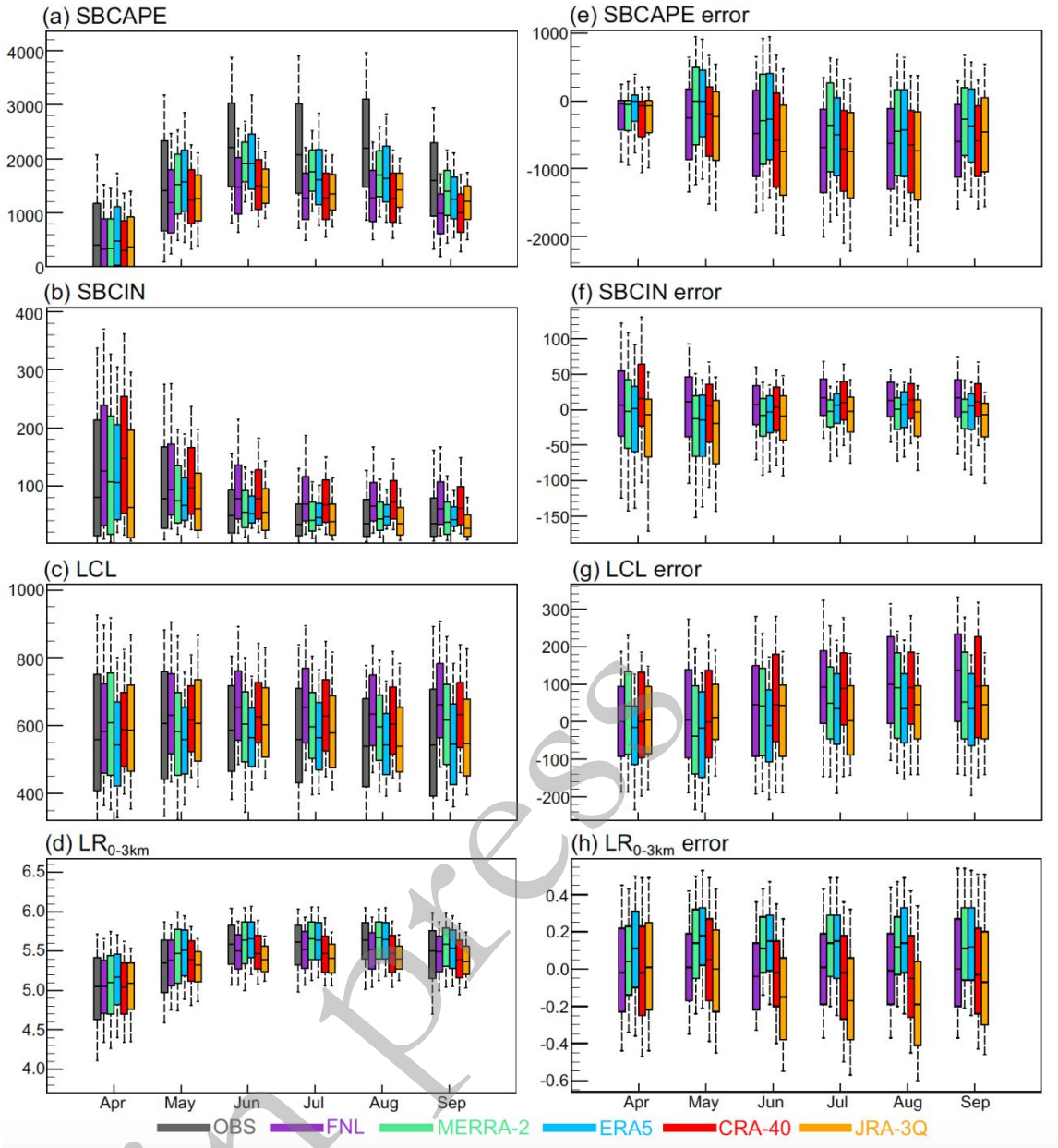

Fig. 3. Comparison of monthly variation of (a) SBCAPE (J kg^{-1}), (b) SBCIN (J kg^{-1}), (c) LCL (m), and (d) $LR_{0\text{-}3km}$ (^{o}C m^{-1}) from the NWP data and the observation, and (e-h) NWP errors respective to the observation (NWP data minus observation).

Comparisons of the monthly variations of dynamic parameters indicate the potential for organized severe weather systems (Fig. 4). Large SRH and deep-layer VWS are found in April, supporting the development of damaging rotating storms such as supercells (Figs. 4a-4b; Davies-Jones et al., 1990). Yet Convection is relatively infrequent in April compared to subsequent months, mostly due to the less favorable thermodynamic environment indicated by SBCAPE (Fig. 3a). From

May to September, low-level mean VWS computed from surface to 1 km and 6 km are around 3.2 m s^{-1} and 6.5 m s^{-1}, respectively. Such VWS (> 5 m s^{-1}; Feng and Zhang 2018) favors the long-lived, moderate speed, moderate size rainfall systems with high rain rates (Baidu et al. 2022).

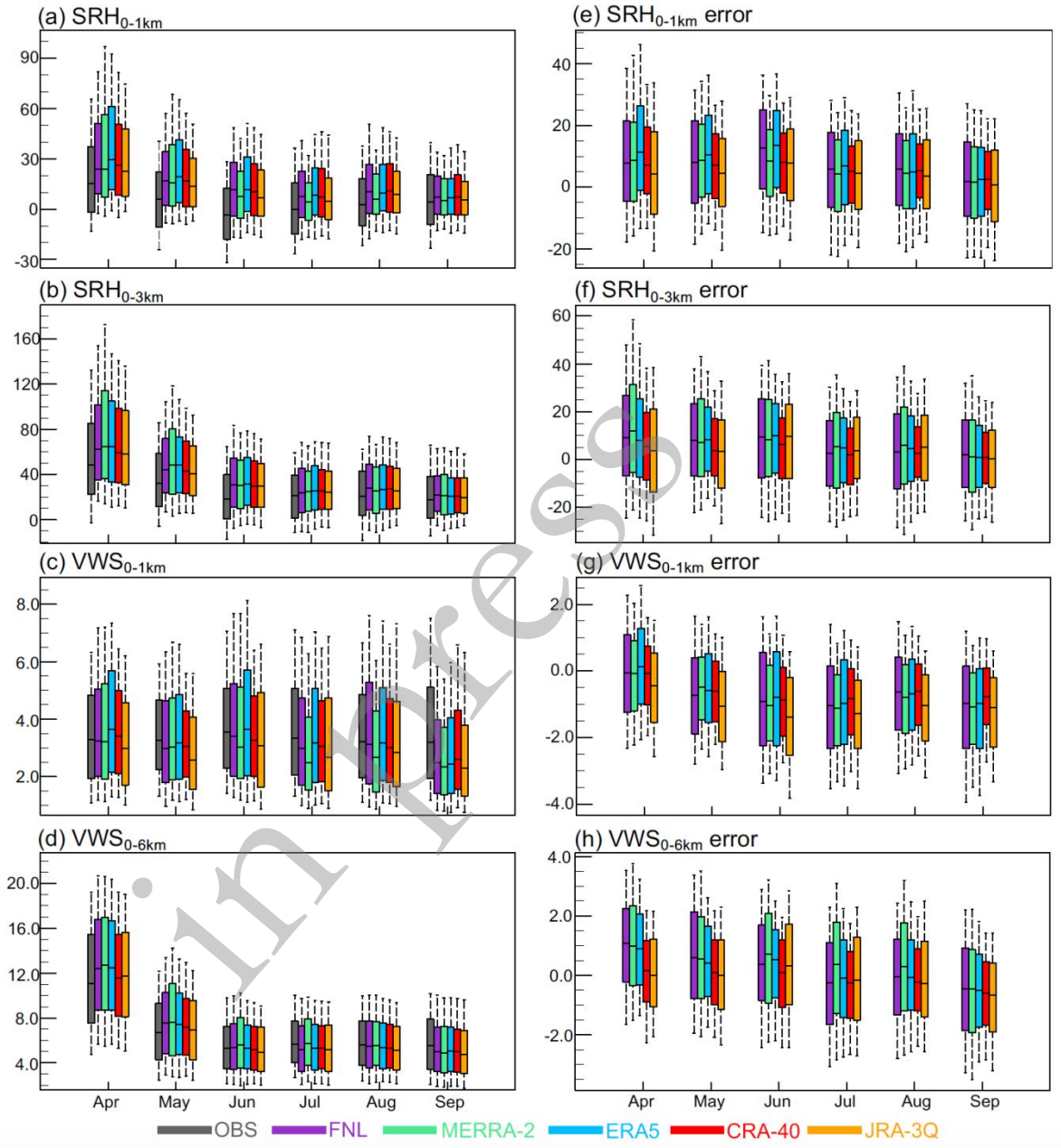

Fig. 4. Similar to Fig. 3, but for (a) and (e) $SRH_{0\text{-}1km}$ (m^2 s^{-2}), (b) and (f) $SRH_{0\text{-}3km}$ (m^2 s^{-2}), (c) and (g) $VWS_{0\text{-}1km}$ (m s^{-1}), and (d) and (h) $VWS_{0\text{-}6km}$ (m s^{-1}).

3.2 Performance of the NWP data

3.2.1. Basic states

The basic states of five global NWP datasets are evaluated against climatological profiles from three radiosonde using mean bias and RMSE (Fig. 5). All NWP data exhibit a negative bias in zonal winds (Fig. 5a) and a positive bias in meridional winds (Fig. 5b) below 925 hPa, decreasing to nearly 0 by 700 hPa, consistent with Yin et al. (2024) and Zhang and Meng (2019). Specifically, zonal winds are underestimated by 0.4–0.6 m s^{-1} and meridional winds overestimated by 0.6–1.0 m s^{-1} below 925 hPa, leading to ~1 m s^{-1} overestimation in wind speeds (Fig. 5c). RMSEs are generally within acceptable limits for assimilation, except for wind direction (Fig. 5d). For thermodynamic state variables, temperature shows a cold bias peaking at 950–925 hPa (Fig. 5e), while humidity errors peaks at 1000 and 900 hPa, with positive biases above 750 hPa (Fig. 5f). The low-level thermodynamic errors are common in global datasets, as seen in ERA-Interim (Allen and Karoly 2014), NCEP/NCAR (Lee 2002), and RUC-2 (Thompson et al. 2003), even with the sounding data was incorporated in the NWP model.

Among the datasets, CRA-40 performs best for dynamic state parameters, showing the highest correlation for U and V wind components, especially above 825 hPa (Table 3), though still biased near the surface (Figs. 5a-b). ERA5 leads in thermodynamic accuracy, especially for water vapor mixing ratio (Qv) below 925 hPa, and provides unbiased Qv profiles above 800 hPa (Fig. 5f). As for temperature, both ERA5 and CRA-40 show strong correlation with the observation at key levels (Table 3), while the MEERA-2 has smaller mean errors below 850 hPa (Fig. 5e, Table 3). In summary, ERA5 best captures nonlinear variable like Qv, while CRA-40 and MERRA-2 excels in linear state variables. Despite these difference, overall deviations are modest, under 0.8 m s^{-1} for U, 0.4 m s^{-1} for V, 1 ^{o}C for temperature, and 1 g kg^{-1} for Qv.

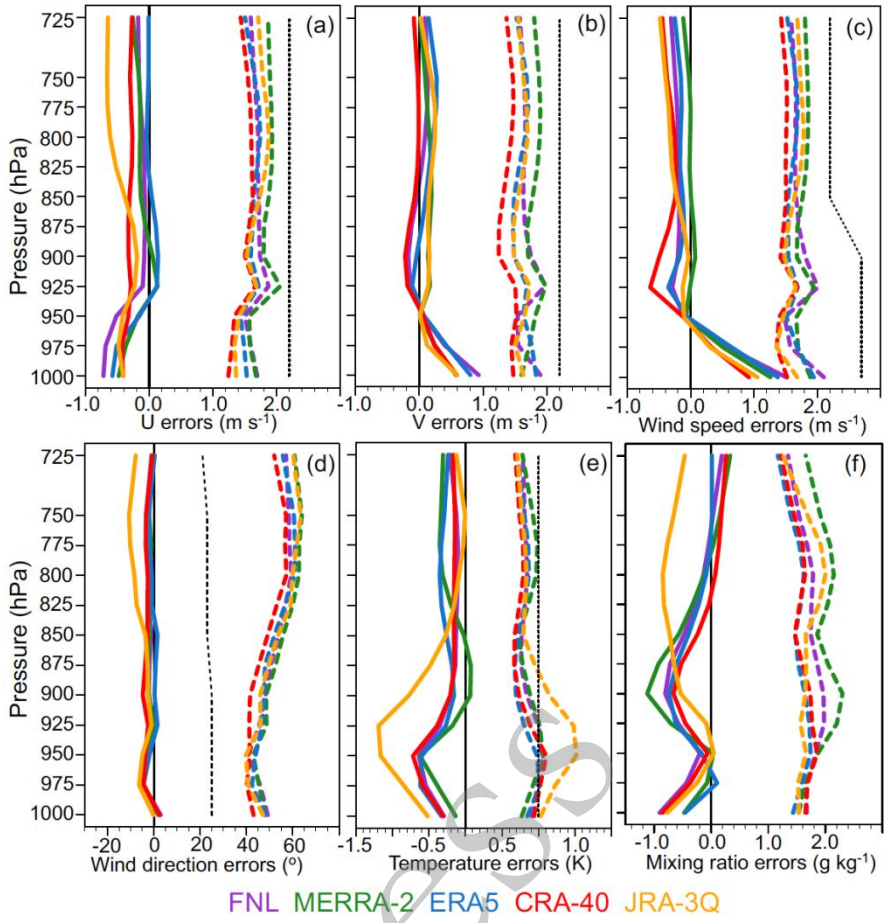

Fig. 5. Vertical profiles of mean errors (solid lines) and RMSE (dashed lines) for (a) zonal winds (m s^{-1}), (b) meridional winds (m s^{-1}), (c) total wind speeds (m s^{-1}), (d) directions (°), (e) temperature (°C), and (f) water vapor mixing ratio (g kg^{-1}). The errors are derived by the difference between NWP soundings and observational soundings (NWP minus observation). The black thick dashed lines in (a)-(e) denote the standard sounding observation errors for the NCEP model (Bao and Zhang 2013).

Table 3. Pearson correlation coefficient, mean absolute error (MAE), and mean error (ME)comparing soundings with collocated FNL, MERRA-2, ERA5, CRA-40, and JRA-3Q for U (m s^{-1}), V (m s^{-1}), T (K), Qv (g kg^{-1}) at 925, 850, and 700 hPa. The best samples are highlighted in **bold**. The correlations have all past the 99% significant test.

		Pearson correlation coefficient					Mean absolute error (MAE)					Mean error (ME)				
		FNL	MERRA-2	ERA5	CRA-40	JRA-3Q	FNL	MERRA-2	ERA5	CRA-40	JRA-3Q	FNL	MERRA-2	ERA5	CRA-40	JRA-3Q
925 hPa	U	0.94	0.93	0.95	**0.96**	0.95	1.31	1.45	1.20	**1.09**	1.18	**-0.10**	0.13	0.12	-0.29	-0.23
	V	0.90	0.90	0.92	**0.94**	0.92	1.36	1.38	1.16	**0.98**	1.19	-0.14	0.17	**-0.11**	-0.18	0.14
	T	0.92	0.92	**0.94**	**0.94**	0.91	0.79	0.77	**0.62**	0.70	1.27	-0.35	**-0.18**	-0.27	-0.39	-1.19
	Qv	0.65	0.62	**0.76**	0.72	0.73	1.53	1.67	**1.31**	1.36	1.17	-0.58	-0.71	-0.62	-0.45	**-0.08**
850 hPa	U	0.95	0.94	0.95	**0.96**	0.95	1.23	1.37	1.16	**1.06**	1.26	-0.07	-0.13	**0.04**	-0.31	-0.38
	V	0.91	0.90	0.92	**0.94**	0.92	1.21	1.32	1.11	**0.92**	1.16	**-0.03**	0.19	0.10	-0.07	0.15
	T	0.93	0.94	0.94	**0.95**	0.89	0.58	0.52	0.54	**0.51**	0.60	-0.13	**-0.02**	-0.26	-0.16	-0.27
	Qv	0.78	0.76	**0.84**	**0.84**	0.76	1.30	1.39	1.08	**1.06**	1.25	-0.47	-0.57	-0.40	**-0.24**	-0.73
700 hPa	U	0.96	0.94	0.96	**0.97**	0.96	1.20	1.39	1.10	**1.00**	1.29	-0.17	-0.26	**-0.01**	-0.27	-0.65
	V	0.93	0.91	0.93	**0.95**	0.93	1.16	1.31	1.10	**0.96**	1.13	0.09	**0.02**	0.15	-0.08	**0.02**
	T	0.85	0.87	0.87	**0.89**	0.86	0.60	0.59	0.54	**0.51**	0.53	-0.21	-0.31	-0.24	-0.17	**-0.12**
	Qv	0.85	0.78	**0.88**	**0.88**	0.87	0.98	1.20	**0.84**	**0.84**	0.95	0.19	0.33	**0.01**	0.26	-0.46

3.2.2. Composite parameters

Thermodynamic performance over the NSCS is first compared to that over Europe and North America. Median error analysis reveals NWP datasets consistently underestimate SBCAPE and overestimate LCL (Fig. 3e, Table 4), aligning with studies over North America (Taszarek et al. 2021; King and Kennedy 2019). In contrast, SBCAPE tends to be overestimated over Europe (Taszarek et al. 2021; Varga et al. 2022), indicating regional variability in NPW accuracy. SBCAPE errors range widely, from near-zero (ERA5) to -297.9 (FNL), indicating substantial uncertainties in this moisture- and temperature-sensitive composite parameter. Uncertainties in SBCIN and LR are even larger and vary with season and dataset.

Further analysis of thermodynamic parameters suggests low-level moisture is the main source of instability uncertainties. NWP datasets simulate temperature more accurately than moisture, with temperature correlations exceed 0.9 at 925-850 hPa and MAE below 0.8 K (except for JRA-3Q) below 700 hPa. In contrast, Qv exhibits weaker correlation (~0.7–0.8) and larger MAE, up to 1.67 g kg $^{-1}$ at 925 hPa (MERRA-2), supporting previous findings that low-level moisture drives instability biases (e.g., Allen and Karoly 2014; Thompson et al. 2003; Lee 2002).

Among the datasets, ERA5 performs best for SBCAPE, with a near-zero median error (Fig. 3e), a ME of -4.95 J kg^{-1}, and a highest correlation (0.65; Table 4), closely followed by MERRA-2, which is plausibly attributed to the better presentation of ERA5 and MERRA-2 on T and Q under 950 hPa (Table 3, Fig. 5). CRA-40, JRA-3Q, and FNL exhibits larger biases, with median errors up to -400 J kg^{-1} and MAEs exceeding 400 J kg^{-1} (Fig. 3e, Table 4). ERA5 also best estimate LCL, while FNL and CRA-40 tend to overestimate it (Fig. 3g), resulting in less favorable condition for convection.

While FNL and CRA-40 generally overestimate the SBCIN, ERA5, MERRA-2 and JRA-3Q display a tendency toward underestimation (Fig. 3f).

while ERA5 tends to perform best for the nonlinear parameters, JRA-3Q, CRA-40 and MERRA-2 perform better for less nonlinear metrics. Specifically, JRA-3Q shows the best performance for EL and LFC, while CRA-40 and MERRA-2 best capture LRs (Table 4). ERA5's strength in capturing moisture- and temperature-dependent parameters is supported by prior studies (e.g., Pilguj et al. 2022; Taszerk et al. 2021), likely due to the its improved representation of moisture related variable especially in lower levels (Fig. 5f, Table 3). This advantage may be attributed to its high horizontal and vertical resolution (Hersbach et al. 2020), improved moisture sensitivity in deep convection (Virman et al. 2021), and assimilation of all-sky satellite observations (Geer et al. 2017).

Statistical analysis shows that NWP performance for dynamic parameters is highly sensitive to layer depth. For SRH, $SRH_{0\text{-}1km}$ exhibit median errors around 6 $m^2 s^{-2}$ and MAEs near 20 $m^2 s^{-2}$ (Table 4), while $SRH_{0\text{-}3km}$ shows similar uncertainty but smaller median errors (Figs. 4e-f). For VWS, deeper layer $VWS_{0\text{-}6km}$ shows little bias (-3 to 3 m s^{-1}), but $VWS_{0\text{-}1km}$ is consistently underestimated (Figs. 4g-h). Correlations between NWP data and observations of the VWS improve with increasing shear layer depth: $VWS_{0\text{-}1km}$ range from 0.59 to 0.76, while $VWS_{0\text{-}6km}$ correlations reach 0.97 (Table 4). MW follows a similar trend that accuracy increases with depth, with correlation rising from 0.88 ($MW_{0\text{-}1km}$) to 0.95 ($MW_{0\text{-}6km}$), and MAE dropping from 0.90 ($MW_{0\text{-}1km}$) to 0.64 ($MW_{0\text{-}6km}$). These results highlight persistent biases in near-surface parameters, likely due to limitations in boundary layer and topographical representation (Allen and Karoly 2014; Taszarek et al. 2018; King and Kennedy 2019).

Among the datasets, CRA-40 performs best for SRH, showing highest correlations (0.88 and 0.92 for $SRH_{0\text{-}1km}$ and $SRH_{0\text{-}3km}$,) and lowest MAEs (18.0 m^2 s^{-2} and 20.0 m^2 s^{-2} for $SRH_{0\text{-}1km}$ and $SRH_{0\text{-}3km}$, respectively). Other datasets slightly overestimate SRH (Figs. 4e-f), exhibit larger MAEs, and show lower correlations (Table 4). CRA-40 also outperforms others in VWS and MW, with strong correlations across all layers: 0.76–0.97 for VWS and 0.90–0.95 for MW (Table 4). Such superior performance of CRA-40 stems from its better simulation of meridional and zonal winds (Table 3). A key factor is CRA-40's enhanced data assimilation, which include not only WMO GTS data, but also additional observations from the CMA, including archived national and regional surface observations, field campaign radiosonde data, and Chinese AMDAR data (Liu et al. 2023). This enhanced data assimilation, particular over oceanic and land regions, substantially improves CRA-40's accuracy at lower levels. However, these enhancements have limited impact on thermodynamic variables, which depend on the full vertical profile.

Further investigation reveals that the performance of NWP data varies significantly across different parameter types, including thermodynamic parameters and dynamic parameters (Tables 3-4). For the thermodynamic parameters, which describe instability based on temperature and moisture profiles, correlations between NWP data and observations are around 0.65 for SBCAPE, 0.60 for SBCIN, 0.8 for LCL, 0.46 for LFC, and 0.89 for EL, with the temperature profiles exhibiting higher correlations (Table 3). In contrast, dynamic parameters derived from wind profiles show even higher correlations, with deeper-layer SRH, VWS and MW exceeding 0.9. These results suggest that NWP data are least reliable for moisture-related parameters, moderately reliable for temperature-related parameter, and most reliable for wind-related parameters. Moreover, for the performance of the

composite parameters, temporal changes are dominated by monthly fluctuations (Figs. 3 and 4) rather than interannual variability (not showed).

Table 4. Similar to Table 2, but for composite parameters.

		Pearson correlation coefficient					Mean absolute error (MAE)					Mean error (ME)				
		FNL	MERRA-2	ERA5	CRA-40	JRA-3Q	FNL	MERRA-2	ERA5	CRA-40	JRA-3Q	FNL	MERRA-2	ERA5	CRA-40	JRA-3Q
Thermodynamic parameters	SBCAPE	0.64	0.65	0.65	**0.66**	0.65	498	446	445	458	**443**	-297.9	-42.66	**4.95**	-272.0	-100.9
	SBCIN	0.60	0.60	0.61	**0.62**	0.61	68.4	65.6	67.4	**60.7**	69.4	13.52	-22.00	-37.99	**0.54**	-50.51
	LCL	0.79	0.80	0.84	0.81	**0.91**	173	157	129	160	**105**	89.41	42.25	**-25.37**	56.08	27.34
	LFC	0.46	**0.49**	0.42	0.46	**0.49**	1150	**980**	1034	1020	981	545.8	-141.5	-220.1	402.9	**-104.9**
	EL	0.89	0.88	0.89	0.88	**0.90**	1482	1265	1229	1365	**1226**	-722.2	-132.4	-155.0	-648.0	**-98.8**
	$LR_{0\text{-}1km}$	0.76	0.77	0.78	**0.80**	0.69	1.20	**1.11**	1.23	1.17	1.57	0.49	**0.39**	0.49	0.41	1.19
	$LR_{0\text{-}3km}$	0.85	**0.86**	**0.86**	**0.86**	0.85	0.37	**0.35**	0.41	0.40	0.39	**0.13**	0.15	0.20	**0.13**	0.16
	$LR_{700\text{-}500hPa}$	0.86	**0.87**	0.86	0.86	0.85	0.41	**0.34**	**0.34**	**0.34**	0.35	0.06	-0.04	0.02	**0.00**	0.16
Dynamic parameters	$SRH_{0\text{-}1km}$	0.80	0.80	0.78	**0.88**	0.81	23.0	23.8	23.2	**18.0**	19.2	6.56	10.62	11.00	7.33	**5.09**
	$SRH_{0\text{-}3km}$	0.90	0.89	0.90	**0.92**	0.89	25.4	29.2	23.6	**20.0**	22.5	5.75	12.73	7.36	3.33	**1.94**
	$VS_{0\text{-}1km}$	0.59	0.62	0.60	**0.76**	0.69	1.85	1.64	1.63	**1.33**	1.51	-0.53	-0.40	**-0.27**	-0.55	-0.74
	$VS_{0\text{-}3km}$	0.88	0.87	0.89	**0.91**	0.90	1.88	2.00	1.68	**1.42**	1.52	**0.02**	0.67	0.18	-0.41	-0.71
	$VS_{0\text{-}6km}$	0.96	0.96	**0.97**	**0.97**	**0.97**	1.88	1.99	1.69	**1.42**	1.45	**0.18**	0.52	0.25	-0.36	-0.33
	$MW_{0\text{-}1km}$	0.88	0.88	**0.91**	0.90	**0.91**	1.14	1.11	1.00	**0.78**	0.89	0.28	0.56	0.47	**0.18**	0.29
	$MW_{0\text{-}3km}$	0.92	0.92	0.92	**0.93**	0.92	0.68	0.72	0.68	**0.55**	0.71	**0.01**	0.20	0.07	-0.08	0.06
	$MW_{0\text{-}6km}$	**0.95**	**0.95**	**0.95**	**0.95**	**0.95**	0.63	0.64	0.58	**0.56**	0.64	-0.19	**-0.00**	-0.07	-0.28	-0.19

4. Impacts of upstream atmospheric errors on downstream convective system

Validation of the CTL showed that simulated daily and diurnal rainfall was stronger than IMERG observation over inland and coastal South China (Fig. 6), consistent with previous studies (Chen et al. 2016; Yang et al. 2004). This overestimation may result from coarser resolution, physics limitations, or misrepresentation of coastal flows (Zhang and Meng 2019). Moreover, CTL uses averaged FNL data and aims to capture general rainfall features, while IMERG reflects real events. Thus, an exact match between CTL-simulated rainfall and satellite-derived rainfall estimates is not expected. Despite differences, CTL successfully reproduces key rainfall patterns, including the timing and location of rainfall anomalies: the late-night to morning positive anomaly of the coastal rainfall (Figs. 6b, 6g, 6e, and 6j), the afternoon positive anomaly of the inland rainfall (Figs. 6c, and 6i), and the centers of total rainfall over both coastal and inland areas.

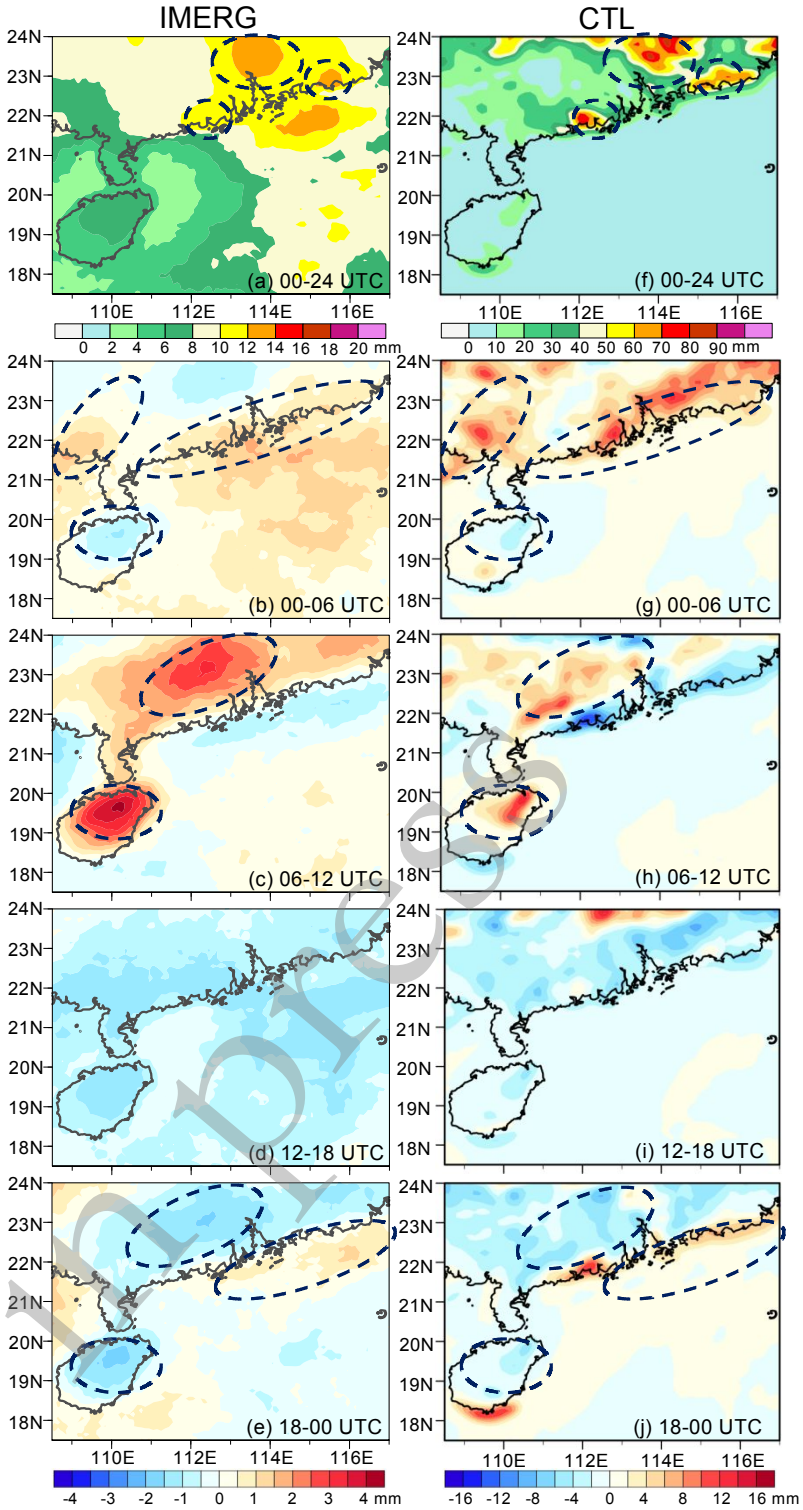

Fig. 6. Comparison between observation (IMERG) and CTL. (a) the daily rainfall averaged from April to September in 2020-2023, (b)-(e) are the diurnal rainfall accumulations every 6 hours. (f)-(j) are similar to (a)-(e), but for CTL. Note that the CTL has been interpolated into IMERG grids.

Comparative analyses of the various sensitivity experiments identify the primary factors contributing to rainfall enhancement in these regions. For the offshore area of south of Hainan island,

experiments involving the reduction of temperature errors show the most significant rainfall enhancement (Figs. 7a, b, d). This rainfall enhancement initiates in the early evening (Figs. 8c, 8g, and 8o) and propagates offshore over the following 12 h (Figs. 8a, 8d, 8e, 8h, 8m, 8p), aligning with the offshore movement of the land breeze. Notably, the FNL tends to underestimate temperature below 700 hPa (Fig. 5e). Consequently, the error reduction procedure increases the low-level vertical temperature gradient over the ocean, leading to two primary effects: 1) enhanced instability over the NSCS, as indicated by increased CAPE (Figs. 9a-9b, and 9d), and moist static energy (MSE; not shown), and 2) intensified land breeze circulations due to a stronger nocturnal land-sea temperature contrast (Huang et al. 2024). These changes result in stronger and earlier coastal rainfall that subsequently propagates offshore. Rainfall production over the offshore regions of east and west coast of South China exhibits similar characteristics and underlying mechanisms.

In contrast, the rainfall enhancement over the inland PRD is mainly attributed to the reduction of errors in dynamic wind fields (Figs. 7a, 7e). Significant rainfall enhancement is observed over the PRD from afternoon to midnight (Figs. 8r-8t), associated with a weakened southerly wind (Fig. 9e), which favors the maintenance of local convection over the PRD region rather than southward propagation (Figs. 6g-i). Additionally, errors in relative humidity have a comparatively smaller impact on rainfall production (Fig. 7c).

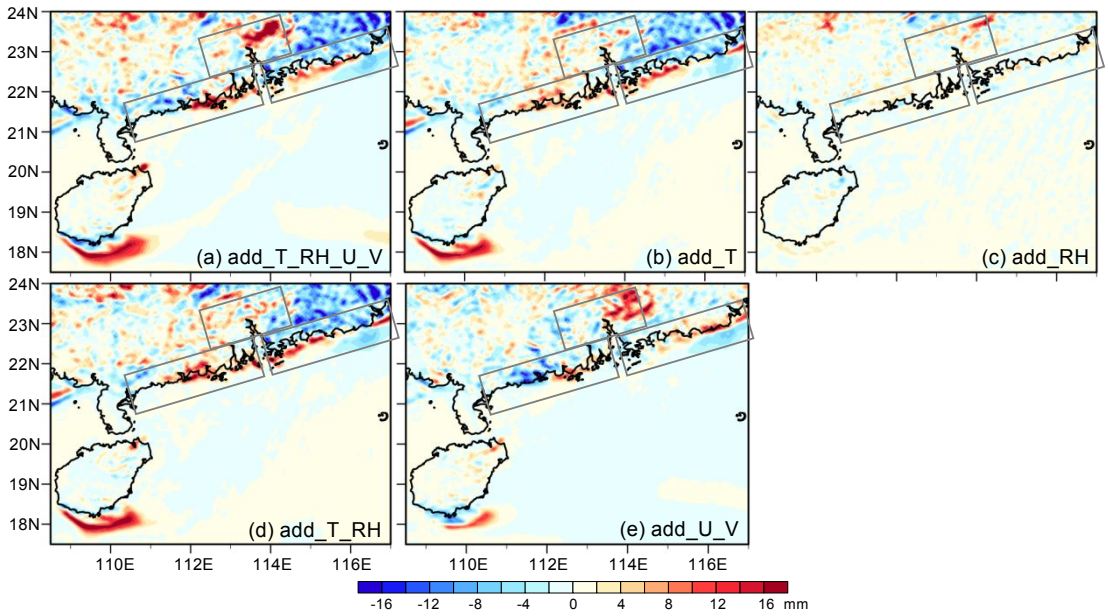

370

371 **Fig. 7.** Difference of daily accumulative precipitation between (a) add_T_RH_U_V, (b) add_T, (c) add_RH, (d)
372 add_T_RH, (e) add_U_V and the CTL. Three grey boxes denote the rainfall hotspot as indicated in Fig. 1a.

373

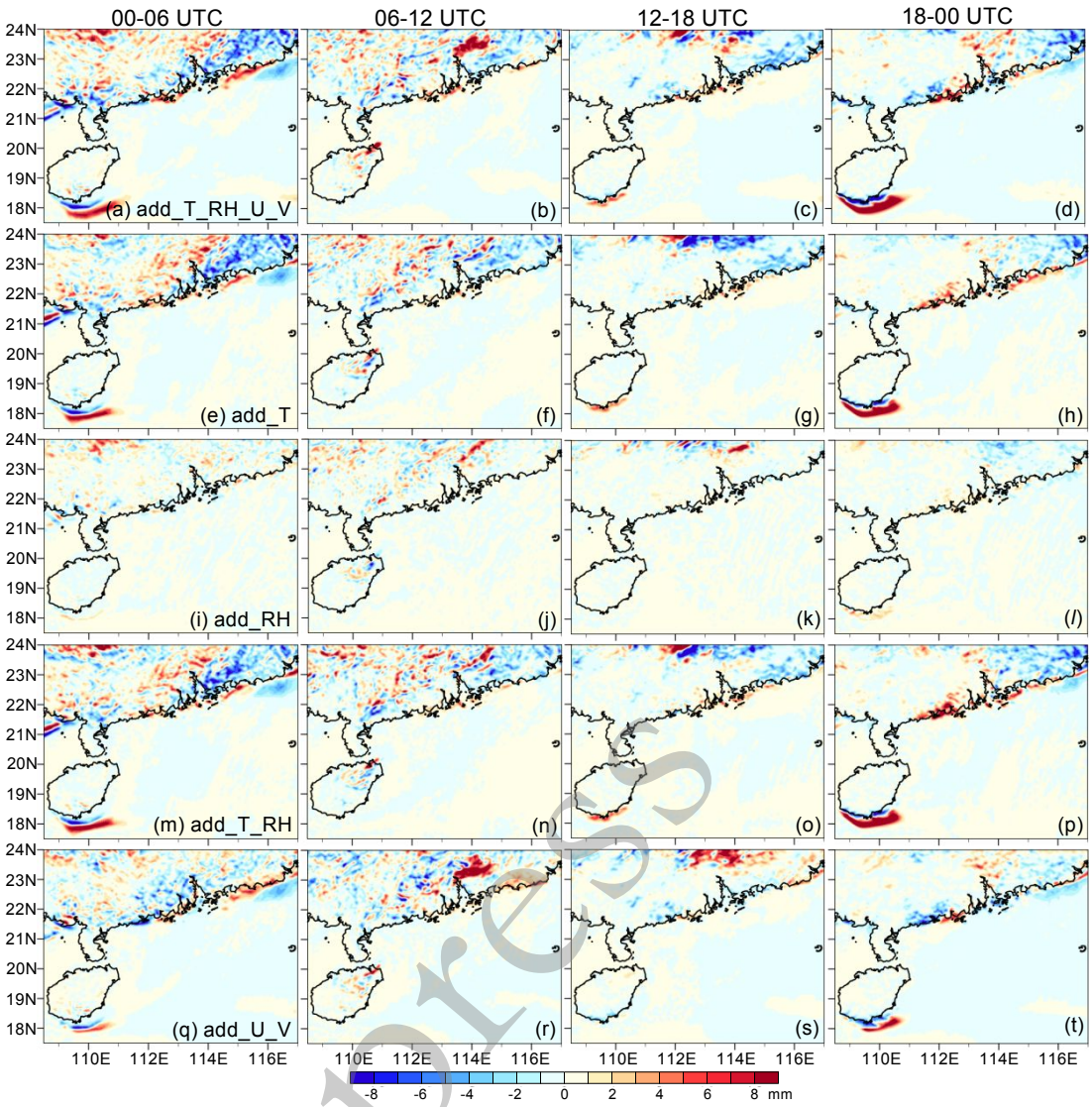

374

375 **Fig. 8.** Difference of diurnal precipitation between (a-d) add_T_RH_U_V, (e-h) add_T, (i-l) add_RH, (m-p)

376 add_T_RH, (q-t) add_U_V and the CTL.

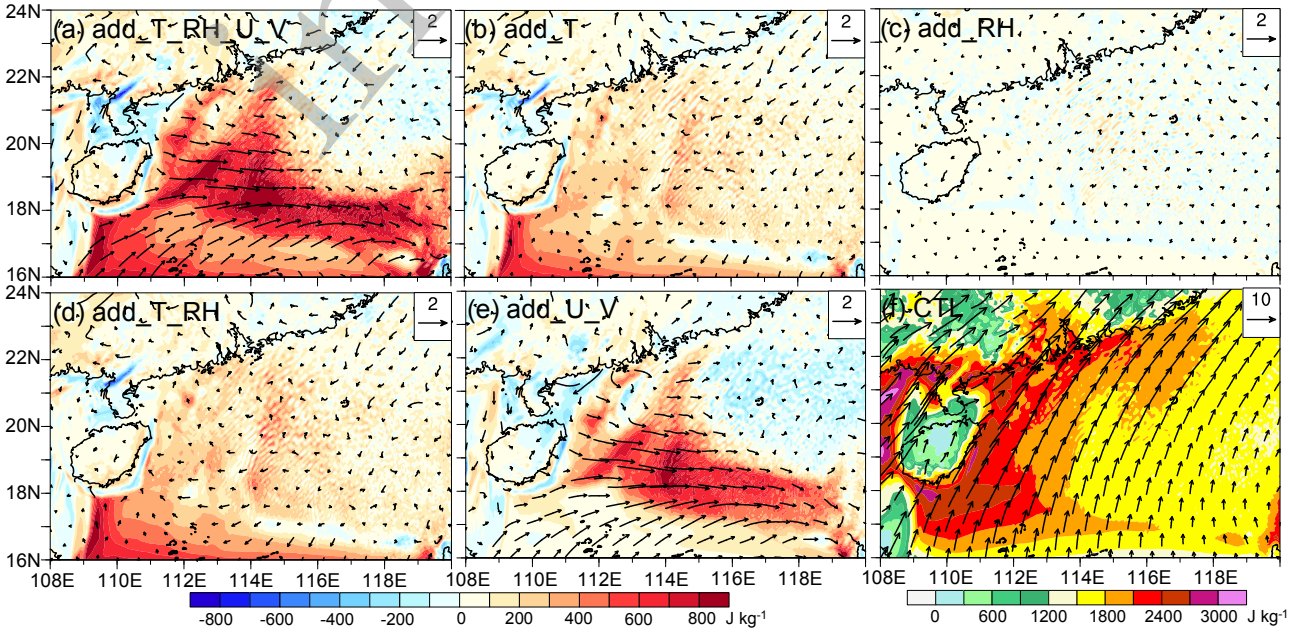

377

Fig. 9. Difference of CAPE and horizontal wind at 925 hPa between (a) add_T_RH_U_V, (b) add_T, (c) add_RH, (d) add_T_RH, (e) add_U_V and the CTL at 00 UTC. (f) is the CAPE from the CTL.

5. Concluding remarks

The coastal regions of southern China experience exceptional convection and its associated rainfall, particularly during warm seasons when lower-tropospheric southerly winds bring moisture and momentum from the NSCS. Due to the sparse observations over the NSCS, NWP models face significant uncertainties. Leveraging long-term radiosonde measurements from NSCS islands, this study characterizes convective environments and evaluates five global NWP datasets (ERA5, MERRA-2, FNL, CRA-40, and JRA-3Q) in representing these conditions.

Systematic biases are revealed in NWP basic state variables below 950 hPa, featuring positive meridional wind biases and negative biases in zonal winds, water vapor mixing ratio, and temperature. The NWP data demonstrate better skill in representing mid-tropospheric lapse rate ($LR_{0\text{-}3km}$, $LR_{700\text{-}500hPa}$), MW, VWS and SRH over deeper layers (e.g., 0-3 km and 0-6 km). These low-level biases lead to underestimation in SBCAPE, and EL, overestimation in LCL, and SRH, and minimal bias in LR, SBCIN, VWS and MW. Moisture-related parameters (SBCAPE, CIN, EL, LCL, LFC) exhibit substantial variability, while LR remains relatively stable. This contrast suggests that the instability errors originate primarily from moisture field inaccuracies rather than temperature discrepancies. Uncertainties among NWP products arise from different model resolutions, sources of the input observations, parameterizations and assimilation methods. Among convective parameters and low-level variables, CRA-40 demonstrates the highest correlation and lowest mean absolute errors for dynamic parameters, while ERA5 performs best in thermodynamic parameters.

Given the systematic biases in NWP model representations of the lower troposphere, multiple

401 sensitivity numerical simulations were conducted to investigate how meteorological variable errors
402 over the NSCS affect downstream rainfall production in coastal regions. The results demonstrate that
403 rainfall patterns are significantly modulated when low-level thermodynamic and dynamic errors over
404 upstream ocean are corrected, particularly over the offshore area of southern Hainan island, coasts of
405 mainland China, and the PRD. The rainfall production on windward coasts is most sensitive to the
406 low-level air temperature errors during nocturnal hours, primarily through enhanced instability and
407 amplified land-sea thermal contrast. The PRD, as a climatological rainfall hotspot, demonstrates
408 strongest sensitivity to low-level wind errors, where weakened southerlies effectively block the
409 southward propagation of inland convective systems. Notably, while higher resolution of WRF
410 simulations tend to produce stronger precipitation forecasts (e.g., Prein et al. 2015), which are also
411 noticed in previous studies that used the same frame work of composite simulation (e.g., Chen et al.
412 2016), this study focuses emphasizes the variation in spatial distributions of the precipitation rather
413 than the absolute rainfall amount of individual synoptic events. The CTL experiment reasonably
414 reproduce the overall rainfall patterns, providing a credible baseline for the sensitivity experiments,
415 which adequately serve the purpose of this investigation.

416 While reanalysis datasets provide valuable insights, notable limitations remain, particularly in
417 the accurate representation of the atmospheric boundary layer. To address these gaps, additional field
418 observations are crucially needed. These efforts should leverage existing observation platforms,
419 including islands, aircrafts and research vessels, to obtained high-resolution, in situ data. Furthermore,
420 targeted field campaign experiments utilizing multi-source observational instruments, deployed on
421 mobile platforms, are anticipated to significantly improve model's depiction of lower-tropospheric

conditions. Such advancements in the model's initial state are essential for enhancing the accuracy of short-term forecasts of severe weather events along the South China coast.

Data availability statement

MERRA-2 data were available at https://disc.gsfc.nasa.gov/. The NCEP FNL data, ERA5 and JRA-3Q data were downloaded at http://rda.ucar.edu. The CRA-40 data were downloaded at http://data.cma.cn/CRA.

Acknowledgments

This research is supported by the National Natural Science Foundation of China (42030610，42275006, 41805035, 42305001), Guangdong Basic and Applied Basic Research Foundation (2024A1515030210), the Guangdong Provincial Marine Meteorology Science Data Center (2024B1212070014), the Open project of Xiamen Key Laboratory of Straits Meteorology (Grants HXQX202304 and 2024KF02), and the Key Innovation Team of China Meteorological Administration (CMA2023ZD08).

References

Allen, J. T., and D. J. Karoly, 2014: A climatology of Australian severe thunderstorm environments 1979–2011: Inter-annual variability and ENSO influence. *Int. J. Climatol.*, **34**, 81–97, https://doi.org/10.1002/joc.3667.

Allen, J. T., and M. K. Tippett, 2015: The characteristics of United States hail reports: 1955–2014. Electron. *J. Severe Storms Meteor.*, **10** (3), https://ejssm.com/ojs/index.php/site/article/view/60/59.

Baidu, M., J. Schwendike, J. Marsham, and J. Bain, 2022: Effects of vertical wind shear on intensities

of mesoscale convective systems over west and central Africa. *Atmos. Sci. Lett.*, **23**, e1094, doi:10.1002/asl.1094.

Bao, X., and F. Zhang, 2013: Evaluation of NCEP–CFSR, NCEP–NCAR, ERA-Interim, and ERA-40 Reanalysis Datasets against Independent Sounding Observations over the Tibetan Plateau. *J. Climate*, **26**, 206–214, https://doi.org/10.1175/JCLI-D-12-00056.1.

Bao, X., R. Xia, Y. Luo, and J. Yue, 2023: Efficiently Improving Ensemble Forecasts of Warm-Sector Heavy Rainfall over Coastal Southern China: Targeted Assimilation to Reduce the Critical Initial Field Errors, *J. Meteor. Res.*, **37**, 486-507.

Chen, F., and J. Dudhia, 2001: Coupling an advanced land surface–hydrology model with the Penn State–NCAR MM5 modeling system. Part I: Model implementation and sensitivity. *Mon. Wea. Rev.*, **129**, 569–585, doi: 10.1175/1520-0493(2001)129<0569:CAALSH>2.0.CO;2.

Chen, J., A. Dai, Y. Zhang, and K. L. Rasmussen, 2020: Changes in convective available potential energy and convective inhibition under global warming. *J. Clim.*, **33**, 2025–2050, https://doi.org/10.1175/JCLI-D-19-0461.1.

Chen, X., F. Zhang, and K. Zhao, 2016: Diurnal Variations of the Land–Sea Breeze and Its Related Precipitation over South China, *J. Atmos. Sci.*, **73**, 4793-4815.

Davies-Jones, R. P., D. W. Burgess, and M. Foster, 1990: Test of helicity as a tornado forecast parameter. Preprints, 16th Conf. on Severe Local Storms, Kananaskis Park, AB, Canada, Amer. Meteor. Soc., 588-592.

462 Davis, S. M., and Coauthors, 2017: Assessment of upper tropo-spheric and stratospheric water vapour
463 and ozone in reanalyses as part of S-RIP. *Atmos. Chem. Phys*., **17**, 12743–12778, https://
464 doi.org/10.5194/acp-17-12743-2017.

465 Ding, Y. H., C.L. Chan, 2005: The East Asia summer monsoon: an overview. *Meteoro. Atmos. Phys.*,
466 **89**, 117-142. doi: 10.1007/s00703-005-0125-z.

467 Du, Y., and G. Chen, 2019: Climatology of Low-Level Jets and Their Impact on Rainfall over
468 Southern China during the Early-Summer Rainy Season, *J. Clim.*, **32**, 8813-8833.

469 Feng, Q., and Q. Zhang, 2018: Statistics of environmental vertical wind shear and water vapor field
470 on the change of tropical cyclone structure in northwest Pacificocean from 2001 to 2014. *Acta*
471 *Scientiarum Naturalium Universitatis Pekinensis*, **54**, 713-720. doi:10.13209/j.0479-
472 0823.2017.141. (in Chinese)

473 Fu, S.-M., J.-P. Zhang, Y.-L. Luo, W.-T. Yang, and J.-H. Sun, 2022: Energy paths that sustain the
474 warm-sector torrential rainfall over South China and their contrasts to the frontal rainfall: A
475 case study, Adv. Atmos. Sci., 39(9), 1519−1535, https://doi.org/10.1007/ s00376-021-1336-z.

476 Gao, X. Y., Y. L. Luo, Y. L. Lin, et al., 2022: A source of WRF simulation error for the early-summer
477 warm-sector heavy rainfall over South China coast: Land-sea thermal contrast in the boundary
478 layer. *J. Geophys. Res. Atmos*., **127**, e2021JD035179, doi:
479 https://doi.org/10.1029/2021JD035179.

480 Geer, A.J., F. Baordo, N. Bormann, S. J. English, M. Kazumori, H. Lawrence, P. Lean, K. Lonitz,
481 and C. Lupu, 2017: The growing impact of satellite observations sensitive to humidity, cloud

and precipitation. *Q. J. Roy. Meteor. Soc*., **143**, 3189–3206. https://doi.org/10.1002/qj.3172.

Gelaro, R., W. McCarty, M. Suarez, et al., 2017: The Modern-Era Retrospective Analysis for Research and Applications, Version 2 (MERRA-2), *J. Clim.*, **30**, 5419–5454, doi: 10.1175/JCLI-D-16-0758.1.

Grell, G. A., and D. Dévényi, 2002: A generalized approach to parameterizing convection combining ensemble and data assimilation techniques. *Geophys. Res. Lett.*, **29**, 1693, doi: 10.1029/2002GL015311.

Harada, Y., S. Kobayashi, K. Y., Kosaka, et al. 2021: Early results of the evaluation of the JRA-3Q reanalysis, EGU General Assembly Conference Abstracts, EGU21-3762, doi: 10.5194/egusphere-egu21-3762.

Hersbach H, Bell B, Berrisford P, et al., 2020: The ERA5 global reanalysis. *Q. J. Roy. Meteorol. Soc.*, **146**, 1999–2049. https://doi.org/10.1002/qj.3803.

Hong, S.-Y., J. Dudhia, and S.-H. Chen, 2004: A revised approach to ice microphysical processes for the bulk parameterization of clouds and precipitation. *Mon. Wea. Rev.*, **132**, 103–120, doi: 10.1175/1520-0493(2004)132<0103:ARATIM>2.0.CO;2.

Hong, S., Y. Noh, and J. Dudhia, 2006: A New Vertical Diffusion Package with an Explicit Treatment of Entrainment Processes. *Mon. Wea. Rev.,* **134**, 2318–2341, https://doi.org/10.1175/MWR3199.1.

Huang, L., and Y. Luo, 2017: Evaluation of quantitative precipitation forecasts by TIGGE ensembles

for south China during the presummer rainy season, *J. Geophys. Res. Atmos*., **122**, 8494–8516, doi:10.1002/2017JD026512.

Huang, L., L. Bai, and Y. Zhang, 2024: Analysis of uncertainties in convection-permitting ensemble simulations of land breeze and nocturnal coastal rainfall in South China. *J. Meteor. Res.*, **38**(6), 1047–1063, doi: 10.1007/s13351-024-4075-0.

King, A. T., and A. D. Kennedy, 2019: North American supercell environments in atmospheric reanalysis and RUC-2. *J. Appl. Meteor. Climatol.*, **58**, 71–92, https://doi.org/10.1175/JAMC-D-18-0015.1.

Kosaka, Y., S. Kobayashi, Y. Harada, C. Kobayashi, H. Naoe, K. Yoshimoto, M. Harada, N. Goto, J. Chiba, K. Miyaoka, R. Sekiguchi, M. Deushi, H. Kamahori, T. Nakaegawa, T. Y. Tanaka, T. Tokuhiro, Y. Sato, Y. Matsushita, and K. Onogi, 2024: The JRA-3Q reanalysis. *J. Meteor. Soc. Japan*, **102**, 49–109, doi:10.2151/jmsj. 2024-004.

Lee, J. W., 2002: Tornado proximity soundings from the NCEP/ NCAR reanalysis data. M.S. thesis, Dept. of Meteorology, University of Oklahoma, 61 pp.

Li, C., and M. Yanai, 1996: The Onset and Interannual Variability of the Asian Summer Monsoon in Relation to Land-Sea Thermal Contrast, *J. Clim.*, **9**, 358-375.

Li, F., D. R. Chavas, K. A. Reed, and D. T. Dawson II, 2020: Climatology of severe local storm environments and synoptic-scale features over North America in ERA5 reanalysis and CAM6 simulation. *J. Clim.*, **33**, 8339–8365, https://doi.org/ 10.1175/JCLI-D-19-0986.1.

520 Li, Z., J. Wei, X. Bao, and Y. Sun, 2023: Intercomparison of Tropospheric and Stratospheric
521 Mesoscale Kinetic Energy Resolved by the High-Resolution Global Reanalysis Datasets, *Q. J.*
522 *Roy. Meteorol. Soc.*, **149**, 3738–3764. doi: https://doi.org/10.1002/qj.4605

523 Liu, Z. Q., L. P. Jiang, C. X. Shi, et al., 2023: CRA-40/Atmosphere—The first-generation Chinese
524 atmospheric reanalysis (1979–2018): System description and performance evaluation. *J.*
525 *Meteor. Res.*, **37**(1), 1–19, doi: 10.1007/s13351-023-208.

526 Manney, G. L., and Coauthors, 2017: Reanalysis comparisons of upper tropospheric-lower
527 stratospheric jets and multiple tro- popauses. *Atmos. Chem. Phys.*, **17**, 11541–11566, https://
528 doi.org/10.5194/acp-17-11541-2017.

529 Markowski, P. M., J. M. Straka, E. N. Rasmussen, and D. O. Blanchard, 1998: Variability of storm-
530 relative helicity during VORTEX. *Mon. Wea. Rev.*, **126**, 2959–2971,
531 https://doi.org/10.1175/15200493(1998)126,2959:VOSRHD.2.0.CO;2.

532 Mlawer, E. J., S. J. Taubman, P. D. Brown, M. J. Iacono, and S. A. Clough, 1997: Radiative transfer
533 for inhomogeneous atmosphere: RRTM, a validated correlated-k model for the longwave. *J.*
534 *Geophys. Res.*, **102**, 16663–16682. https://doi.org/10.1029/97JD00237

535 National Centers for Environmental Prediction/National Weather Service/NOAA/U.S. Department
536 of Commerce. 2000, updated daily. NCEP FNL Operational Model Global Tropospheric
537 Analyses, continuing from July 1999. Research Data Archive at the National Center for
538 Atmospheric Research, Computational and Information Systems Laboratory.
539 https://doi.org/10.5065/D6M043C6.

Niu, G. Y., Z. L. Yang, K. E. Mitchell, et al., 2011: The community Noah land surface model with multiparameterization options (Noah-MP): 1. Model description and evaluation with local-scale measurements. *J. Geophys. Res. Atmos*., **116**, D12109, doi: 10.1029/2010JD015139.

Pilguj, N., M. Taszarek, J, Allen, et al. 2022: Are trends in convective parameters over the united states and Europe consistent between reanalyses and observations? *J. Clim.*, **35**, 3605-3636.

Prein, A., W. Langhans, G. Fosser, et al. 2015: A review on regional convection-permitting climate modeling: Demonstrations, prospects, and challenges, Review of Geophysics, 53,323–361, doi:10.1002/2014RG000475.

Rädler, A. T., P. Groenemeijer, E. Faust, and R. Sausen, 2018: Detecting severe weather trends using an Additive Regressive Convective Hazard Model (AR-CHaMo). *J. Appl.Meteor. Climatol.*, **57**, 569–587, https://doi.org/10.1175/JAMC-D-17-0132.1.

Skamarock, W., and Coauthors, 2008: A description of the Advanced Research WRF version 3. NCAR Tech. Note TN-4751STR, 113 pp. [Available online at http://www.mmm.ucar.edu/wrf/users/docs/arw_v3_bw.pdf.]

Sun, J., and F. Zhang, 2012: Impacts of mountain–plains solenoid on diurnal variations of rainfalls along the mei-yu front over the east China plains. *Mon. Wea. Rev.*, **140**, 379–397, doi:10.1175/MWR-D-11-00041.1.

Sun, J.-H., Y.-C. Zhang, R.-X. Liu, S.-M. Fu, and F.-Y. Tian, 2019: A review of research on warm-sector heavy rainfall in China. Adv. Atmos. Sci., 36, 1299−1307, https://doi.org/10.1007/s00376-019-9021-1.

560 Shen, C., J. L. Zha, J. Wu, D. M. Zhao, C. Azorin-Molina, W. X. Fan, Y. Yu, 2022: Does CRA-40
561 outperform other reanalysis products in evaluating near-surface wind speed changes over China?
562 *Atmos. Res.*, **266**, 105948, https://doi.org/10.1016/j.atmosres.2021.105948.

563 Taszarek, M., H. Brooks, and B. Czernecki, 2017: Sounding-Derived Parameters Associated with
564 Convective Hazards in Europe, *Mon. Wea. Rev*., **145**, 1151-1528.

565 Taszarek, M., H. E. Brooks, B. Czernecki, P. Szuster, and K. Fortuniak, 2018: Climatological Aspects
566 of Convective Parameters over Europe: A Comparison of ERA-Interim and Sounding Data. *J.*
567 *Clim.*, **31**, 4281–4308, https://doi.org/10.1175/JCLI-D-17-0596.1.

568 Taszarek, M., J. T. Allen, T. Púcik, K. Hoogewind, and H. E. Brooks, 2020: Severe convective storms
569 across Europe and the United States. Part II: ERA5 environments associated with lightning,
570 large hail, severe wind and tornadoes. *J. Clim.*, **33**, 10263–10286, https://doi.org/10.1175/JCLI-
571 D-20-0346.1.

572 Taszarek, M., N. Pilguj, J. T. Allen, V. Gensini, H. E. Brooks, and P. Szuster, 2021: Comparison of
573 Convective Parameters Derived from ERA5 and MERRA-2 with Rawinsonde Data over
574 Europe and North America. *J. Clim.*, **34**, 3211–3237, https://doi.org/10.1175/JCLI-D-20-
575 0484.1.

576 Thompson, R. L., R. Edwards, J. A. Hart, K. L. Elmore, and P. Markowski, 2003: Close proximity
577 soundings within supercell environments obtained from the Rapid Update Cycle. *Wea.*
578 *Forecasting*, **18**, 1243–1261, https://doi.org/10.1175/1520-
579 0434(2003)018,1243:CPSWSE.2.0.CO;2.

580 Tippett, P. W., C. Lepore, and J. E. Cohen, 2016: More tornadoes in the most extreme US tornado
581 outbreaks. *Science*, **354**, 1419–1423, https://doi.org/10.1126/science.aah7393.

582 Toptill, D., and D. J. Kirshbaum, 2022: Ensemble Sensitivity of Precipitation Type to Initial
583 Conditions for a Major Freezing Rain Event in Montreal. *Mon. Wea. Rev.*, **150**, 1761–1780,
584 https://doi.org/10.1175/MWR-D-21-0254.1.

585 Varga, A., and H. Breuer, 2022: Evaluation of convective parameters derived from pressure level and
586 native ERA5 data and different resolution WRF climate simulations over Central Europe, *Clim.*
587 *Dyn.*, **58**, 1569-1585, https://doi.org/10.1007/s00382-021-05979-3.

588 Virman, M., M. Bister, J. R*ä*is*ä*nen, et al. 2021: Radiosonde comparison of ERA5 and ERA-Interim
589 reanalysis datasets over tropical oceans, *Tells A*, **73**, 1929752,
590 https://doi.org/10.1080/16000870.2021.1929752.

591 Wu, J., J. Guo, Y. Yun, et al., 2024: Can ERA5 reanalysis data characterize the pre-storm environment?
592 *Atmos. Res*., **297**, 107108. https://doi.org/10.1016/j.atmosres.2023.107108.

593 Yang, J., Huang, M. & Zhai, P., 2021: Performance of the CRA-40/Land, CMFD, and ERA-Interim
594 Datasets in Reflecting Changes in Surface Air Temperature over the Tibetan Plateau. *J.*
595 *Meteorol. Res.*, **35**, 663–672. https://doi.org/10.1007/s13351-021-0196-x.

596 Yang, M.-J., B. J. D. Jou, S.-C. Wang, J.-S. Hong, P.-L. Lin, J.-H. Teng, and H.-C. Lin, 2004:
597 Ensemble prediction of rainfall during the 2000–2002 mei-yu seasons: Evaluation over the
598 Taiwan area. *J. Geophys. Res.*, **109**, D18203, doi:10.1029/2003JD004368.

599 Yin, J., X. Liang, Y. Xie, et al. 2023: East Asia Reanalysis System (EARS), *Earth Syst. Sci. Data*,

15, 2329–2346.

Yu, X., L. Zhang, T. Zhou, et al., 2021: The Asian Subtropical Westerly Jet Stream in CRA-40, ERA5, and CFSR Reanalysis Data: Comparative Assessment. *J. Meteorol. Res.,* **35**, 46–63. https://doi.org/10.1007/s13351-021-0107-1.

Zhang, M., and Z. Meng, 2019: Warm-Sector Heavy Rainfall in Southern China and Its WRF Simulation Evaluation: A Low-Level-Jet Perspective. *Mon. Wea. Rev.*, **147**, 4461–4480, https://doi.org/10.1175/MWR-D-19-0110.1.

Zhang, J., T. Zhao, Z. Li, et al., 2021: Evaluation of Surface Relative Humidity in China from the CRA-40 and Current Reanalyses. *Adv. Atmos. Sci.*, **38**, 1958–1976. https://doi.org/10.1007/s00376-021-0333-6.

Zhou, Z., S. Chen, Z. Li, Y. Luo, 2023: An Evaluation of CRA40 and ERA5 Precipitation Products over China. *Remote Sens.*, **15**, 5300. https://doi.org/10.3390/rs15225300